[110] tensile testing of single crystalline gold thin films with nanotwins: In situ TEM and XRD studies

P. Godard, F. Mompiou, Julien Drieu La Rochelle, M. Drouet, C. Mocuta, Dominique Thiaudière, Y F Woguem, A. George, D. Eyidi, Anny Michel, et al.

[110] tensile testing of single crystalline gold thin films with nanotwins: *In situ* TEM and XRD studies

P. Godard,[1,*] F. Mompiou,[2] J. Drieu La Rochelle,[1] M. Drouet,[1] C. Mocuta,[3] D. Thiaudière,[3] Y. F. Woguem,[1] A. George,[1] D. Eyidi,[1] A. Michel,[1] J. Durinck,[1] S. Brochard,[1] and P. O. Renault[1]

[1]*Université de Poitiers - CNRS - ENSMA, 11 Boulevard Marie et Pierre Curie, 86073 Poitiers, France*

[2]*CEMES-CNRS, Université de Toulouse, 29 rue J. Marvig, 31055 Toulouse, France*

[3]*Synchrotron SOLEIL, L'Orme des Merisiers, Départementale 128, 91190 Saint-Aubin, France*

(Received 17 April 2025; accepted 28 August 2025; published 8 October 2025)

Tensile tests of 50-nm-thick single-crystalline (001) gold thin films containing nanotwins are monitored *in situ* with x-ray diffraction (XRD) and transmission electron microscopy (TEM). It is argued that for uniaxial tensile tests along the [110] direction, the induced average stress in the films during loading hardly depends on whether they are deposited onto a polymeric substrate (for XRD) or free-standing (for TEM). When straining along this direction, XRD experiments show an impressive ≈500% increase in the twin volume for two favorably twin orientations at an applied strain of only 4.0%. Furthermore, the twin volume increase is accompanied by a twin rotation. Submicron scale TEM observations show that the increase in volume is correlated with the glide of partial dislocations, either along the coherent twin boundaries (TB) or at the incoherent TBs, or close to microstructure imperfections. In the last case, twins coalesce and acquire a micrometer size. An intense dislocation activity occurs in these large twins, still increasing the strain concentration and resulting in crack expansion. The multiplicity of plasticity mechanisms suggests that the twinning quantification may significantly depend on the initial defect type (twins, dislocations, nanometric holes) and density. The twin rotation is also observed postmortem in TEM. However, the XRD data analysis shows that twinning is not the only plasticity mechanism: first, the yield point of the film supported on a substrate is ≈0.5%, but the twinning starts only at 1.0%, and, second, at an applied strain of 4.0%, the plastic strain induced by the twin is less than 0.8%.

DOI: 10.1103/s5l4-z48r

I. INTRODUCTION

Published in 2004, the seminal paper of L. Lu *et al.* showed that submicrometric grain-sized nanotwinned (NT) copper samples present exceptional mechanical resistance, good ductility, and an electrical resistivity close to that of coarse-grained metals [1]. Since then, many studies have concentrated on the influence of twin thickness λ (i.e., the distance between the coherent twin boundaries, or CTBs) reporting, e.g., a maximal strength at $\lambda = 15$ nm in Cu [2], a continuous increase of strength down to $\lambda = 2.9$ nm (at the expense of ductility) in Ni [3] or from $\lambda > 1$ μm to 15 nm in Ag [4]. The importance of the grain size d has also been studied, e.g., a very high hardness was found in Ag for $\lambda < 7$ nm and $d = 50$ nm [5]. This dependence on λ and d indicates that plasticity mechanisms are controlled by both twin and grain boundaries (GBs). In particular, the importance of GBs as dislocation sources in NT metals was emphasized [6]. Early GB cracking induced by GB sliding was predicted in Ni when $\lambda < 6$ nm and $d = 20$ nm [7]. Moreover, common plasticity mechanisms were observed in Ni, Cu, Ag, and Al, like jogged dislocations that expand across all CTBs for very small λ and threading dislocations that glide between two CTBs when $\lambda > 5$ nm [7]. It was also shown that the stability of GBs and of TBs in Cu was increased via the introduction of Cr impurities that segregate at the CTBs kinks [8] or with W nanoparticles [9].

In addition to the growth twins mentioned above, deformation twins appear as an alternative to dislocations, particularly in single crystals [10–14]. Electron microscopy and molecular dynamics simulations were combined in studies of the tensile strain of gold {110} nanowires [15,16]. The stress-strain curves clearly depended on the defect content of the samples: nanowires of high crystalline quality exhibited numerous active dislocation sources that created many small twins; smooth stress-strain curves resulted. On the other hand, nanowires with rough surfaces contained nucleation sites for partial dislocations; the emission of these dislocations induced steps at the surface, which ultimately led to large twins, localized plasticity, and early stress drops. In the latter case, twin coalescence was observed, and the twins grew until they met an obstacle like a twin in a conjugate slip plane, which stopped the plasticity and led to sample fracture. In another study on gold {110} nanowires, cyclic compression-tension tests were applied. During the first compression, only perfect dislocations appeared. Then, twinning occurred in tension, and detwinning in compression [17].

The study of twinning in gold thin films has a long history [18]. J.W. Matthews studied in [19] single-crystalline (001) metallic thin films strained along [100] and along [110]. Twinning was observed in both cases through the extension

*Contact author: pierre.godard@univ-poitiers.fr

of growth twins. Moreover, the twinning induced a thinning of the film, and this entailed an early failure of the sample. The impact of the film thickness on the flow stress of gold single crystals loaded along [100] was assessed by P. Gruber *et al.* with synchrotron x-ray diffraction (XRD) [20]. The flow stress increased by a factor of 6 when the thickness decreased from 850 to 50 nm, and then stabilized or slightly decreased to 31 nm. However, the microstructure was not homogeneous, as the thinnest films contained holes and more twins. Concerning the second point, during sample elaboration, twins grew from the interface with the substrate. As the films thickened, some twins intersected other twins, and some twins ended before the film surface with an incoherent twin boundary (ITB); as a result, fewer twins crossed the entire film thickness. Note that the films were supported on a compliant substrate; the load was applied to the substrate, along a direction that corresponds to [100] in the crystalline film.

The plasticity mechanisms occurring in gold single-crystal (001) films with twins were thoroughly studied in [21], for thicknesses ranging from 40 to 160 nm. The [100] loading was monitored by *in situ* transmission electron microscopy (TEM). The multiplication of dislocations was rarely observed. Dislocation nucleation was generally localized close to defects (nanoparticles in epitaxy with the film at the surface, twin boundaries, or holes for the thinnest films). The authors also showed that the thinnest films deformed mainly by the glide of isolated partial dislocations or perfect dislocations; these were highly curved and frequently underwent cross-slip. The thickest films had straight, perfect dislocations, which left segments at the interface with the polymeric substrate during their glide. At large deformation, they glided in the noncompact {001} planes.

In this paper, we combine different *in situ* approaches in order to better understand deformation mechanisms in gold thin films containing a single crystalline matrix and nanotwins. Two complementary techniques were used: *in situ* XRD to calculate the stress applied to the sample and the twin volume evolution through pole figures, and *in situ* TEM to observe the key plasticity mechanisms. Though these mechanisms are not described at an atomic scale, the combination of the two techniques makes it possible to quantify and interpret the microstructure evolution. Moreover, while XRD gives the sample behavior in areas over $(100\,\mu\text{m})^2$ large, the submicrometric TEM observations show that this behavior results from different mechanisms, developing in the present case in homogeneous matrix areas and close to cracks.

Pole figures give quantitative information on the grain orientations in a sample. They were used to study, for instance, anisotropic growth of thin films [22], pseudoelasticity in shape memory alloys [23], twinning during shock compression in polycrystals [24] or single crystals [25]. We are not aware of any XRD pole figures taken *in situ* in NT samples, apart from the previous study from our group [26]. *In situ* TEM allows the direct observation of the plasticity mechanisms at the nanoscale [27]. During mechanical tests, it showed the existence of stable single-arm sources in submicrometric samples [28], the emission of partial dislocations at surface steps in samples smaller than 10 nm [29], or CTBs sliding and migrating [30]. Concerning polycrystalline NT samples, N. Lu *et al.* observed two types of TB-dislocation interactions,

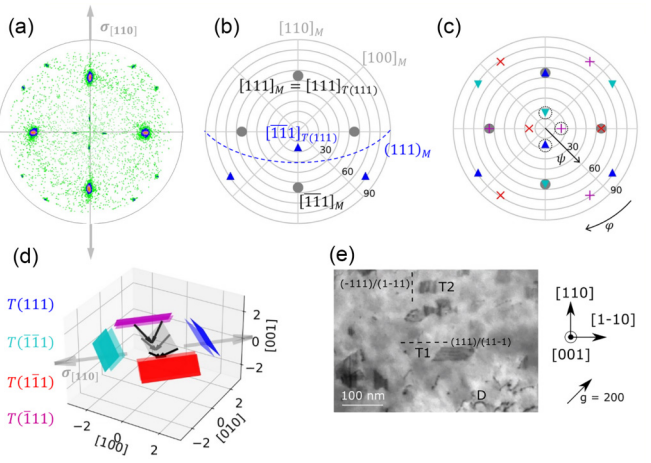

FIG. 1. (a) Experimental {111} pole figure before loading test. The center of the figure is [001]. It shows four main peaks, corresponding to the matrix, and small spots associated to the twins. (b) Sketch showing the orientation relationship between the matrix (gray disks) and a $T(111)$ twin (blue triangles): the [111] poles are coincident while the three others are symmetric with respect to the (111) plane. (c) Sketch corresponding to the complete pole figure when considering the four poles of each crystalline orientation (the matrix and the four twin families). The circled poles are the ones analyzed in Figs. 2 and 3. (d) Representation in sample space of the coherent twin boundaries of each twin family. The light gray arrows represent the loading direction; the other arrows indicate the Burgers vectors of the slip systems with the highest Schmid factors for a [110] loading (in black for perfect dislocations, dark gray for partials, see Sec. 4.4 for details). (e) Bright field image of the initial microstructure; the beam direction was perpendicular to the foil plane, and the diffraction vector was $\vec{g} = 200$. Contrasts with horizontal fringes like T1 are from the $T(111)$ or $T(\bar{1}\bar{1}1)$ twin families; contrasts with vertical fringes like T2 belong to $T(\bar{1}11)$ or $T(1\bar{1}1)$. One also observes many dislocations, like the one exemplified with a D.

depending on the twin size [31]. This was confirmed in [32] for grain sizes over 10 nm, with a critical twin thickness that was grain size dependent.

The XRD analysis of the present article is based on the same data as in [26]. Methods are detailed in Sec. II, results are presented in Sec. III, and discussed in Sec. IV.

II. METHODS

A. Sample preparation and microstructure

The gold thin films were elaborated by Ar beam sputtering at a sufficient temperature to obtain an orientation epitaxy between the (001) NaCl substrates and the gold deposit. By dissolving the salt into water, the 50-nm-thick films were transferred onto 50 μm-thick polyimide films (Kapton®) with cruciform shapes for the XRD experiments or a copper grid for the TEM measurements. The orientation of the thin film with respect to the polyimide or copper grid determined the load direction. More details can be found in [26]. A {111} pole figure taken before the mechanical tests is shown in Fig. 1(a); a matrix-twin relationship is exemplified in Fig. 1(b); and each

spot of the full pole figure is attributed to a grain orientation in Fig. 1(c).

The four possible matrix-twin relationships with 180° rotations along the different ⟨111⟩ directions appear; the films thus contain four twin families, and we denote by $T(hkl)$ the twin family obtained by a twist along $[hkl]$. We remark that the CTB separating a $T(111)$ twin and the matrix has a (111) orientation, and similarly for twins in the other families, Fig. 1(d). Let us finally note that the twin families split into two sets: the $T(111)$ and $T(\bar{1}\bar{1}1)$ families whose CTBs normals project onto the (001) plane along the load direction, and the $T(\bar{1}11)$ and $T(1\bar{1}1)$ families whose CTBs contain the load direction, see Fig. 1(d). Figure A-1 in the Supplemental Material (SM) illustrates the different crystallographic directions contained in a section of a matrix $(1\bar{1}0)$ plane [33].

Figure 1(e) shows a bright field (BF) image of the microstructure of the film before straining. It was obtained using a $\vec{g} = 200$ diffraction vector with a film surface plane perpendicular to the electron beam. At a larger scale, a few porosities can be evidenced. The microstructure seen here is composed of nanotwins and perfect dislocations. Twins appear in projection about 35 nm wide and 30 to 100 nm nm long. Their long facets correspond to CTBs in one of the four {111} plane families, all inclined at 55° from the film normal. Because of the projection effect, the $T(111)$ and $T(\bar{1}\bar{1}1)$ families are indistinguishable and oriented in the image along the $[1\bar{1}0]$ direction (horizontal in Fig. 1(e), see, e.g., T1) while the $T(\bar{1}11)$ and $T(1\bar{1}1)$ families are oriented along the [110] direction (vertical, like T2). When viewed in cross section, the twins are about 6 nm thick, and their height equals the height of the films [26]. Hence, in plane view, the twinned volume cannot be observed because it overlaps with the matrix, and the contrast of the nanotwin is similar to that of stacking faults with thickness fringes. The end parts of the twin correspond to ITBs.

B. *In situ* XRD

The *in situ* XRD measurements were made at the DiffAbs beamline of the synchrotron radiation source SOLEIL [34]. The x-ray beam had an energy of 9.000 keV, a divergence of $0.20° \times 0.014°$, and an intensity full width at half-maximum of about 300×270 μm^2 (horizontal times vertical). The detector was an XPAD S140 [35,36], which, when located at 621 mm from the sample, offers a field of view of $\approx 7° \times 4°$ around the {111} reciprocal lattice nodes. The installation of a biaxial tensile tester is possible on the six-circle goniometer, as described in [37]. This machine loads the four arms of the cruciform substrate by pairs, so that a large range of strain ratios can be achieved.

The pole figures were obtained at a scattering angle of $2\theta^{111} = 34°$, thus probing the {111} lattice spacing. The polar angle ψ was varied from 0 to 81° while the azimuthal angle ϕ range extends over 210°. The exposure time was 0.1 s. Only three twin families appeared in the truncated pole figures; nevertheless, taking into account the symmetry of the straining directions with respect to the crystallographic orientations, the behavior of representative elements in each twin family was captured. The analysis of the data was similar to the one described in [38].

The macroscopic strains were measured by digital image correlation (Corelli software [39]), thanks to an optical camera placed below the substrate [37].

Choosing the sample coordinate system with z along the normal of the thin film, x and y respectively along and perpendicular to the straining direction, 24 pole figures were recorded up to a strain $\varepsilon_{s,xx}$ of 4%, while $\varepsilon_{s,yy}$ was kept smaller than 0.2% during the whole tests—as shown in SM 1 and discussed in Sec. 4.1, a uniaxial strain test in gold along [110] leads to an applied stress very close to being uniaxial along [110]. Then, an unloading down to 2% in seven steps was applied; the sample did not remain flat during further unloading. While straining, the strain rate was 0.06 s^{-1}, but the recording of a pole figure took ≈30 min. To avoid sample drift, the strains were measured with respect to a 10 N equibiaxial pretension reference state.

C. *In situ* TEM

The 50 nm gold films were transferred from NaCl to copper grids with 80×80 μm^2 holes, that were then glued on a straining grid fitting between the two grips of the straining holder. The presence of a grid with relatively small holes slowed down the cracking of the film.

A JEOL 2010 microscope operating at 200 kV and equipped with a LaB_6 source was used for the *in situ* experiments. Uniaxial load tests were performed using a Gatan straining holder (model 654). Video stills were recorded by an SIS Megaview III camera, with a 688×516 resolution and a recording rate of 25 images per second. Furthermore, postmortem automated crystallographic orientation mapping was performed using the ASTAR system on a CM20FEG microscope operated at 200 kV using electron precession. 6×1 μm^2 maps were recorded using a step size of 10 nm and a spot size less than 10 nm so that patterns did not overlap.

III. RESULTS

A. *In situ* XRD

The twin volume evolution is probed through the integration of the signal around the poles located at $\psi = 16°$, after background subtraction. These poles are chosen because they are (i) at a low declination angle, and so weakly affected by defocalization, and (ii) far from matrix poles. The background was a linear interpolation, for each pole and at each applied strain, of the intensity measured at $\phi = \pm 15°$ away from the pole. As already shown in Ref. [26], the [110] straining direction distinguishes two sets of twin families, Fig. 2.

On the one hand, the $T(\bar{1}11)$ family shows a moderate decrease of 20%; by symmetry (Fig. 1), we suppose that the $T(1\bar{1}1)$ family has the same behavior. On the other hand, the $T(111)$ and $T(\bar{1}\bar{1}1)$ families (whose intersection between their CTBs and the film surface is perpendicular to the strain direction) show an impressive 400 to 500% increase at an applied strain of only 4%. We also observe that the increase starts only at $\varepsilon \approx 1.0\%$, and becomes linear after $\varepsilon \approx 1.5\%$. Finally, when unloading, the volume of the $T(111)$ and $T(\bar{1}\bar{1}1)$ twin families starts to decrease at $\varepsilon \approx 3.0\%$. While straining the film, streaks develop in the radial directions of the pole figures for twins in the $T(111)$ and $T(\bar{1}\bar{1}1)$ families.

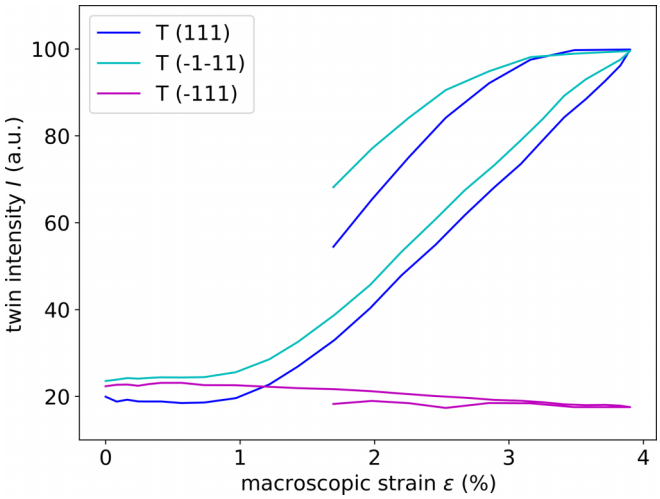

FIG. 2. Integration of the scattered intensity around the twin poles measured in *in situ* XRD for a [110] straining test; the legend corresponds to twin families [see Figs. 1(c) and 1(d)] and not to diffraction peaks.

The streaks go from the twin poles at $\psi = 16^\circ$ to higher values. To show them, line cuts in the pole figures are shown in Fig. 3.

These streaks evidence a rotation of the twins along the $[1\bar{1}0]$ direction; the angle between their CTBs and the surface, initially of 55°, decreases. The schematic in SM Fig. A-1 illustrates this rotation in sample space. We note from Figs. 2 and 3 that each twin family had (at least partly) reversible twin volume and twin orientation evolutions. The use of a two-dimensional detector allows tracking the angular position of the Bragg peak during the test. From this, we deduce the elastic strain along the [111], $[1\bar{1}1]$, and $[\bar{1}\bar{1}1]$ directions in the matrix. The results are shown in Fig. 4.

We observe an elastic regime up to $\varepsilon \approx 0.5\%$ (the first six measurements fit a straight line), and a slow decrease of the strain after 1.5%.

Because the film was plastically elongated during the loading and was adherent to a substrate with a high yield point, it entered into a compressive state during the unloading. The unloading steps were then too large to unambiguously determine the elastic limit. The macroscopic strain $\varepsilon \approx 3.0\%$, where detwinning of the $T(111)$ and $T(\bar{1}\bar{1}1)$ twin families started, corresponds to an elastic strain $\varepsilon^{(111)} = \varepsilon^{(\bar{1}\bar{1}1)} \approx -0.20\%$.

B. *In situ* TEM

Figure 5(a) shows a BF image at the early straining stage taken with $\vec{g} = 1\bar{1}1$, i.e., with the foil sample inclined 32° around the [110] direction.It shows two long nanotwins of the $T(111)$ family. Twinning dislocations visible in particular at the tip were identified as $1/6[\bar{1}\bar{1}2]$ Shockley partials using the extinction criterion ($\vec{g} \cdot \vec{b} = 0$ when $\vec{g} = 3\bar{1}1$). The alternate dark and bright contrasts, highlighted in the zoomed view, are typical of groups of Shockley partials gliding in adjacent planes [40]. Upon further straining, different mechanisms can be evidenced. The first one corresponds to dislocation emission from twins. Figures 5(b) and 5(c) present two snapshots and an image difference that highlights motions. In Fig. 5(b),

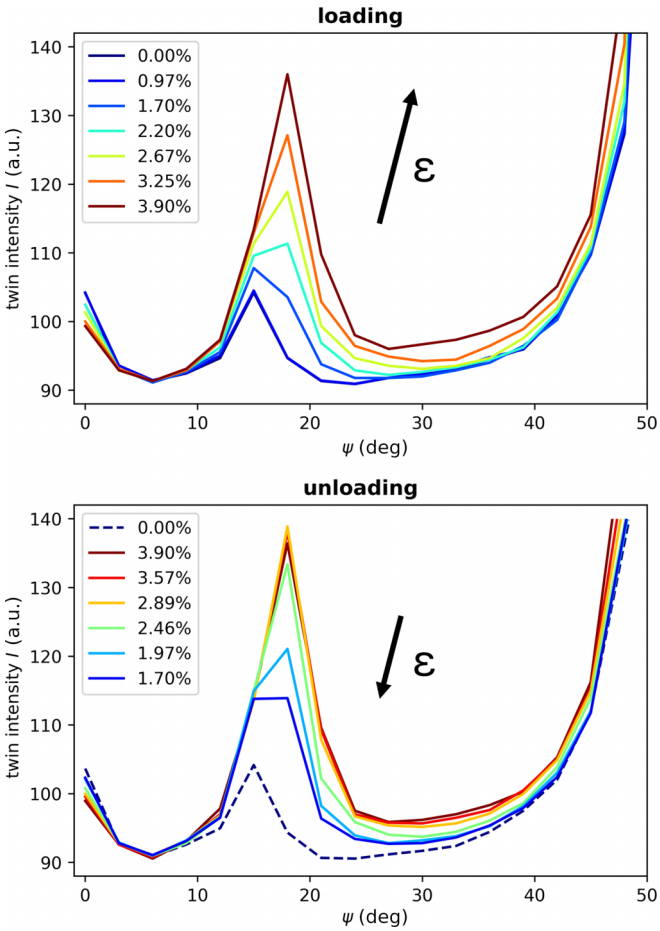

FIG. 3. Line cuts from the pole figures to show the twin rotation during loading (top panel) and unloading (bottom). The peak at 16° comes from the (111) planes of the $T(\bar{1}\bar{1}1)$ twin family; the peak from the (111) planes of the matrix is at 55°. During loading, the curve corresponding to $\varepsilon = 0.97\%$ is superimposed with the one at $\varepsilon = 0\%$. The curve before the test is shown in a dashed line in the unloading panel for comparison.

a perfect $1/2\langle 110\rangle$ type dislocation moves either in the (111) or $(\bar{1}\bar{1}1)$ plane ahead of the nanotwin. This observation is reminiscent of the emissary dislocations observed in α-iron [41] that accommodate deformation ahead of twins. Surprisingly, some perfect dislocations were found emitted from the twin and gliding in the $(1\bar{1}1)$ or $(\bar{1}11)$ planes [i.e., gliding vertically, as in Fig. 5(c)], although the resolved shear stress is supposed to be low for these slip systems (Table A-1). Figure 6 shows two series of snapshots illustrating mechanisms leading to nanotwin lengthening and thickening; this concerns twins from the $T(111)$ and/or $T(\bar{1}\bar{1}1)$ families, and corresponds thus to the twin volume increase in the XRD data.

In Fig. 6(a), a first group (1) of Shockley partials is emitted ahead of a twin $T1$ from the $T(111)$ or $T(\bar{1}\bar{1}1)$ family, viewed horizontally. It eventually interacts with another nanotwin $T2$, viewed vertically. The first partials are then stopped and pushed by a second (2) and a third (3) group of Shockley partials gliding in parallel planes, leading to the formation of a pileup. The first group eventually overcomes the twin and escapes rapidly. During the Shockley dislocation motion,

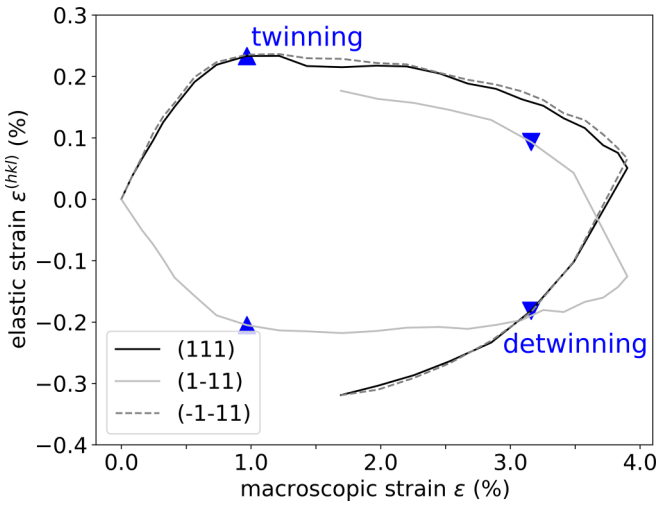

FIG. 4. Elastic strain in the matrix, probed with different {111} diffraction peaks, that is, along different directions in sample space. The points where, according to Fig. 2, twinning (▲ symbols) and detwinning (▼) appear in the $T(111)$ and $T(\bar{1}\bar{1}1)$ twin families are noted.

the twin length of $T1$ increases in the $[\bar{1}10]$ direction. The collective motion of twinning dislocations in parallel planes also increases twin thickness in the [111] or $[\bar{1}\bar{1}1]$ direction by an amount equal to $a/\sqrt{3}$ per dislocation, a being the lattice parameter. That the partials belong to adjacent planes cannot be inferred from the images, but is deduced from the similarity with [40]. Moreover, this is corroborated by the twin thickening that has been observed in XRD, during pause in *in situ* TEM, and postmortem (see below). Figure 6(b) highlights the interaction of moving Shockley partials (1) with a perfect dislocation D. Here again the motion of the Shockley dislocations is blocked temporarily by D leading to the piling of the partial dislocations (note the thinning of the black contrast indicating the shortening of the distance between the partials). The dislocation D eventually reacts with the partials, which become free again to move. The details of the interaction cannot be interpreted here, but may lead to a sessile dislocation in the twin plane. Overall, nanotwin growth is a major deformation mechanism, in particular because it is able to overcome blocking dislocations and other existing nanotwins. The lengthening of twins from the $T(111)$ and/or $T(\bar{1}\bar{1}1)$ families is also evidenced in Fig. 7.

It was observed either homogeneously (away from any crack tips), as highlighted in Fig. 7(a), showing the lengthening of several nanotwins in the $\pm[\bar{1}10]$ directions, or, for larger twins, close to porosities or crack tips, as displayed in Fig. 7(b). Figure 7(b) shows first the nucleation and lengthening of two parallel nanotwins (marked by red arrows), followed by the rapid propagation of a larger twin $T0$ by the motion of a sharp tip. Here, the twinned area is large enough to reveal in projection the two CTBs delineated by the white dashed lines. Observations at a larger scale reveal indeed the presence of several micron-long deformation twins, in most cases in front of crack tips. Figures 8(a) and 8(b) show two twins with lengths equal to 7 and 21 μm, respectively, and up to 4 μm large. An enlarged view of the right part of one of these twins is shown in Fig. 8(c). The twinned area appears highly deformed with a high dislocation density. Elongated contrasted areas marked by arrows can also be evidenced. They probably correspond to some matrix area retained during the growth and coalescence of nanotwins. Finally, a postmortem crystallographic orientation map was obtained in an area containing a large twin. Figure 9(a) shows a BF image of the twin that emerges from a crack on the left.

Figure 9(b) is an inverse pole figure along the normal to the foil, which hence corresponds to the [001] direction for the matrix and $[22\bar{1}]$ for the twin. Contrary to the BF image, which is strongly impacted by local elastic distortions around the twin, the orientation map clearly reveals the twin shape. It forms an elongated needle, less than 100 nm thick at the tip and about 500 nm at the base, close to the crack. It is, in fact, composed at its extremity of two tips, and this is reminiscent of the coalescence of two parallel twins. Interestingly, the orientation in the twin changes from one end to the other (from positions 1 to 3). This corresponds to a rotation along $[\bar{1}10]$ with an increasing angle, as shown by the cumulative rotation angle in Fig. 9(c). The twin rotation and its axis are in agreement with the XRD data presented in the previous subsection. Describing the theoretical twin orientation as the one obtained from the matrix with a rotation of 109.5° around $[\bar{1}10]$, the misorientation between the twin and the matrix (3–3') is 103.8° close to the twin tip, about 6° away from a perfect twin orientation. Close to the crack (1–1'), it is about 86.8°, which, taking into account the matrix rotation by a few degrees, is close to a $\Sigma 17a$ GB.

IV. DISCUSSION

A. Average applied strain and stress fields in supported and free-standing films

In the XRD experiment, the stress field applied to the film was dictated by the strain imposed on the substrate: indeed, we showed in [42,43] that the in-plane strain components are fully transmitted from the substrate to the film, no matter the elastic anisotropy of the latter. In the present experiment, we applied a force along $[1\bar{1}0]$ to cancel the Poisson effect and obtain an in-plane strain ratio $\varepsilon_{s,yy}/\varepsilon_{s,xx} = \varepsilon_{[1\bar{1}0]}/\varepsilon_{[110]} \approx 0$. We show with Eq. (A-7) in SM A.1.2 that under these conditions, the in-plane stress ratio satisfies $R_\sigma := \sigma_{s,yy}/\sigma_{s,xx} \approx -0.028$.

In the TEM experiment, the film was freestanding. The applied stress was uniaxial, so $R_\sigma = 0$. The comparison between the two applied stress ratios shows that a [110] uniaxial strain test (as obtained with the biaxial machine) and a [110] uniaxial load test (as in freestanding films) are very similar. This is confirmed with the Schmid factors, given for the two tests in columns B and D of Table A-1.

Given the gold stiffness coefficients, this similarity is specific to the [110] direction. For example, we show with Eq. (A-5) in SM A.1.2 that $R_\sigma \approx 0.46$ for a uniaxial [100] strain test. In the previous studies of single-crystalline gold thin films deposited onto a polyimide [20,21], uniaxial stresses were applied to the substrate along the [100] direction of the film. In this case, the in-plane stress-ratio is $R_\sigma \approx 0.14$, SM A.1.3. In other words, a uniaxial stress test on the substrate imposes a biaxial stress on the film, and a uniaxial

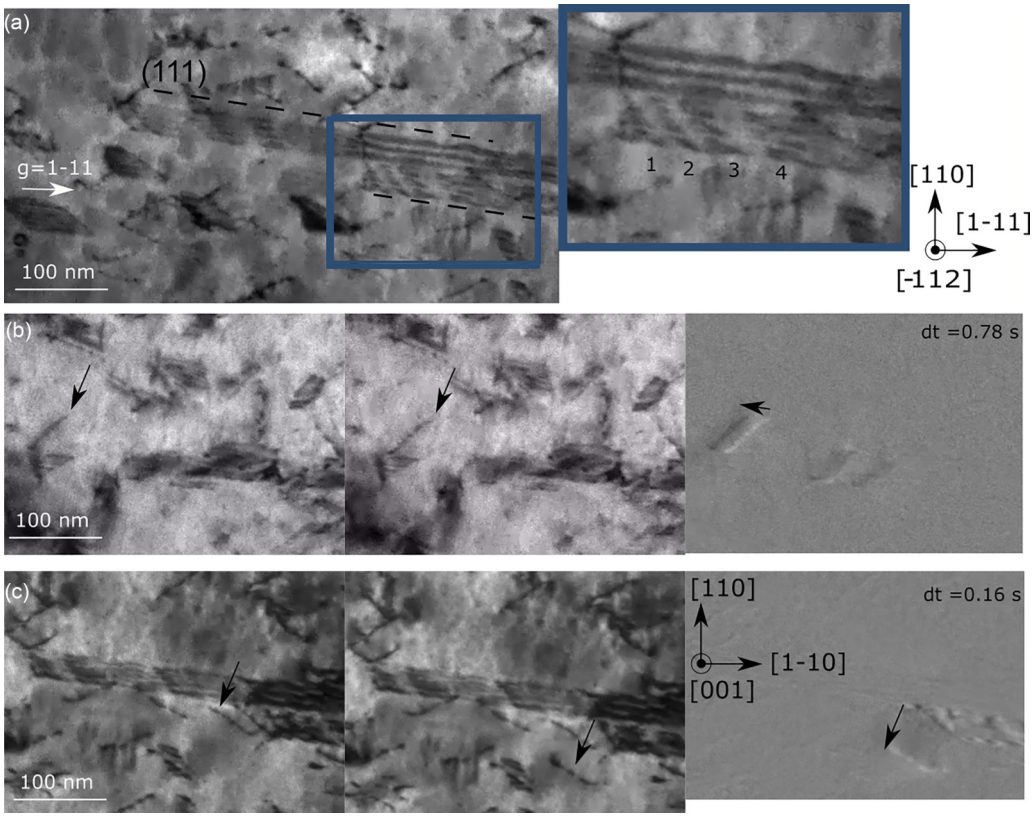

FIG. 5. (a) Two nanotwin tips observed at early straining, viewed inclined 32° from the foil surface with $\vec{g} = 1\bar{1}1$. In the insert, four groups of Shockley partials (1–4) are highlighted. (b) and (c) Examples at further straining of dislocation emission (indicated by arrows) ahead of the nanotwin tips. Left and middle: two BF images taken with a time interval dt; right: the corresponding image difference. The coordinate system shown in (c) applies to (b) as well.

tensile tester may impose on supported films stress ratios R_σ quite different from 0.

Finally, the uniaxial strain tests imposed in our XRD experiments avoid the development of buckles parallel to the loading direction, as is seen when comparing the optical images from [44] and [45].

B. Mechanical resistance

P. Gruber *et al.* measured, for a supported 53 nm thin film loaded along [100], a longitudinal flow stress of ≈500 to 600 MPa, and a lateral flow stress of ≈100 to 150 MPa [20]. The ratio is close to the linear elasticity prediction given in the previous subsection, $R_\sigma \approx 0.14$. In our case, the maximum elastic strain was $\varepsilon^{(111)} = 0.24\%$ (Fig. 4); from Eqs. (A-14) and (A-7) in the SM, we deduce longitudinal strain and stress values of $\varepsilon_{s,xx} \approx 2.6 \times 2.4\,10^{-3} \approx 6.1\,10^{-3}$ and $\sigma_{s,xx} \approx$ 500 MPa. The maximum stress values in [20] and the present work were thus similar, even if, besides the mechanical tests, the twin configurations were very different; indeed, in [20], the twins were, before the test, already micrometer long, and often ran from one hole to another one.

We are not aware of any previous studies on the strength of gold single-crystalline thin films loaded along [110]. However, in nanowire geometry, the authors of [46] or [15] obtained a maximum stress of ≈1600 MPa, though the flow stress was 200 MPa [46] and 400 to 700 MPa [15] when large twins developed.

C. Elastic energy density

When a strain is applied to a bicrystal, the elastic anisotropy can drive grain boundary migration [47,48]. In particular, H. Xie *et al.* correlated in [49] the migration of a {112} ITB with the elastic energy stored in the two crystalline orientations. The {112} ITB consists of a set of partial dislocations whose Burgers vectors sum to zero. In other words, the ITB migration did not contribute to a macroscopic strain but led to a state of lower energy due to the elastic anisotropy. We examine in this subsection whether the twin volume evolution could be induced by such a phenomenon. The elastic energy density $U = \frac{1}{2}\epsilon_{ij}\sigma_{ij}$ is computed for a given strain and straining direction in homogeneous single crystals having the crystallographic orientation of the matrix or of the twins. The coefficients of the gold stiffness tensor are given in SM A.1.2. The orientation is indicated with θ, the rotation angle between [100] and the straining direction, here orthogonal to [001]. U was computed in the matrix thanks to the hypothesis of vanishing stress normal to the surface: $\sigma_{s,zz} = 0$. An arbitrary applied strain $\varepsilon_{s,xx} = 1\%$ has been chosen, but the ratios obtained are independent of it. The result is shown in Fig. 10, where the fourfold symmetry of the [001] axis has been used to limit θ to [0, 90°].

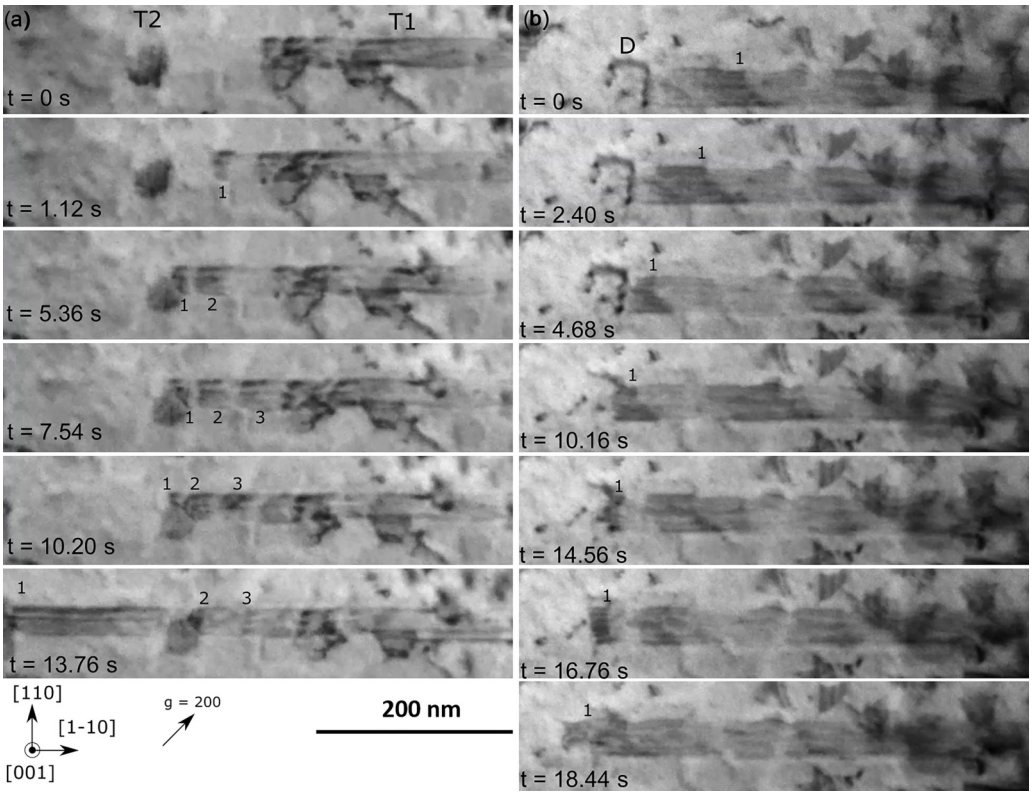

FIG. 6. BF images showing in (a) the propagation of Shockley partials (1–3) along a nanotwin (T1) and their interaction with a grown-in nanotwin (T2), and in (b) the interaction between Shockley partials (1) and a perfect dislocation D.

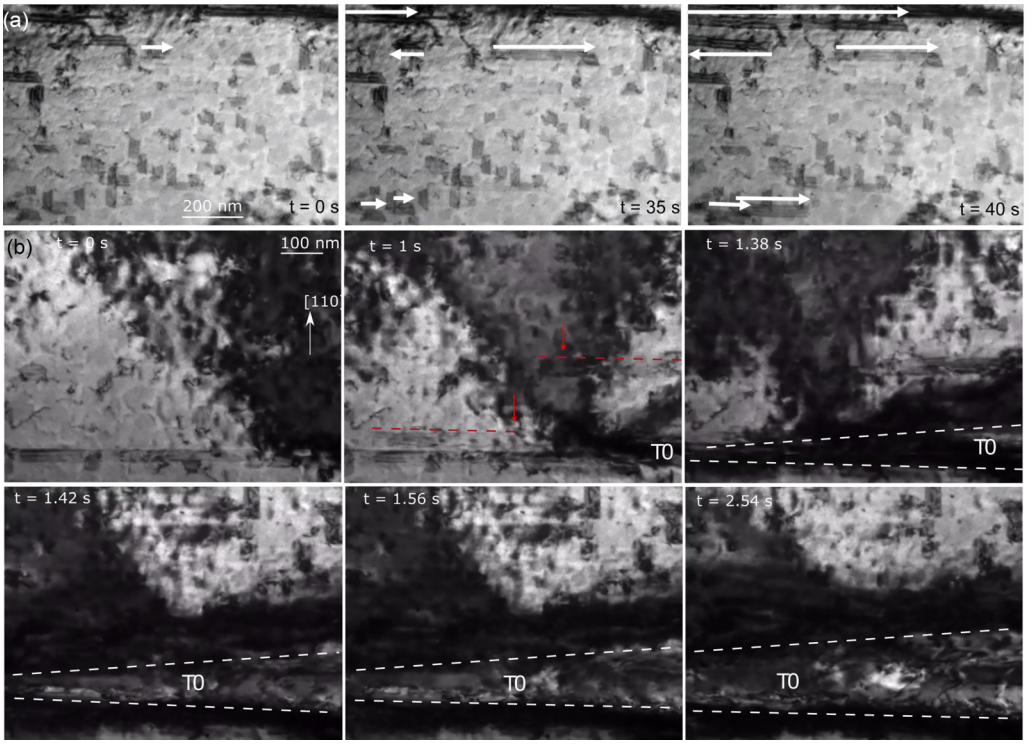

FIG. 7. (a) BF images taken at different times showing the lengthening of several parallel nanotwins under stress (white arrows). (b) A series of images highlighting the nucleation of nanotwins (red dashed lines) and the expansion of a large twin $T0$ whose CTBs are marked by white dashed lines. The coordinate system is the same as in Fig. 6.

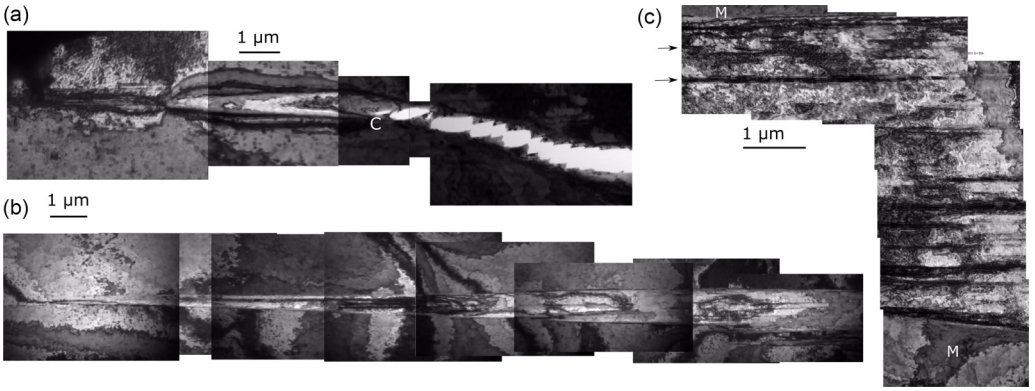

FIG. 8. (a) Overview showing a large twin ahead of a ductile crack. C is the crack tip. (b) A microtwin with a sharp tip. (c) Zoom in of the largest area of (b) showing a highly deformed area in the twin, compared to the original matrix (M). Note the presence of trapped elongated regions in the twin indicated by arrows.

It is seen that, for the matrix, the [100] and [110] straining directions are the two extreme cases: [100] is the straining direction that costs the least energy, while [110] ($\theta = 45°$) requires the most energy. The difference is significant, with a ratio of $2.7/4.0 = 0.67$.

We also computed the elastic energy density in the twins, still using the $\sigma_{s,zz} = 0$ hypothesis (which is an approximation for thin twins [50]). Because ε_s is invariant with respect to 180° rotations around [001], the elastic energy density is equal in the $T(111)$ and $T(\bar{1}\bar{1}1)$ twin families, as well as in the $T(\bar{1}11)$ and $T(1\bar{1}1)$ twin families. There is a degenerate case when $\theta = 0°$, that is, for a [100] straining, where the four twin families have equal behaviors. The results are also plotted in Fig. 10; the values of the two sets of twin families are interchanged when $\theta \in [90, 180]°$.

In any case, considering samples with (001) planes parallel to the surface, it is more expensive in energy to elastically deform a twin than the matrix. When θ belongs to $[0, 90]°$, we note that the elastic energy density in the $T(\bar{1}11)$ and $T(1\bar{1}1)$ twin families weakly depends on the straining direction, in contrast to the other two twin families. In particular, a [110] straining induces a value of U that is 28% lower in the $T(111)$ and $T(\bar{1}\bar{1}1)$ twin families than in the others.

A [100] straining of the sample induces an elastic energy 2.4 higher in the twins than in the matrix; for a [110] straining, the ratio is 1.2 for the twins that grew up in the *in situ* experiments, and 1.6 for those that slightly decreased (according to the XRD data). More generally, since U is smaller in the matrix than in any twin, the elastic energy imposed by any $[hk0]$ straining cannot be the driving force for twinning; this is thus different from what happened with the sample

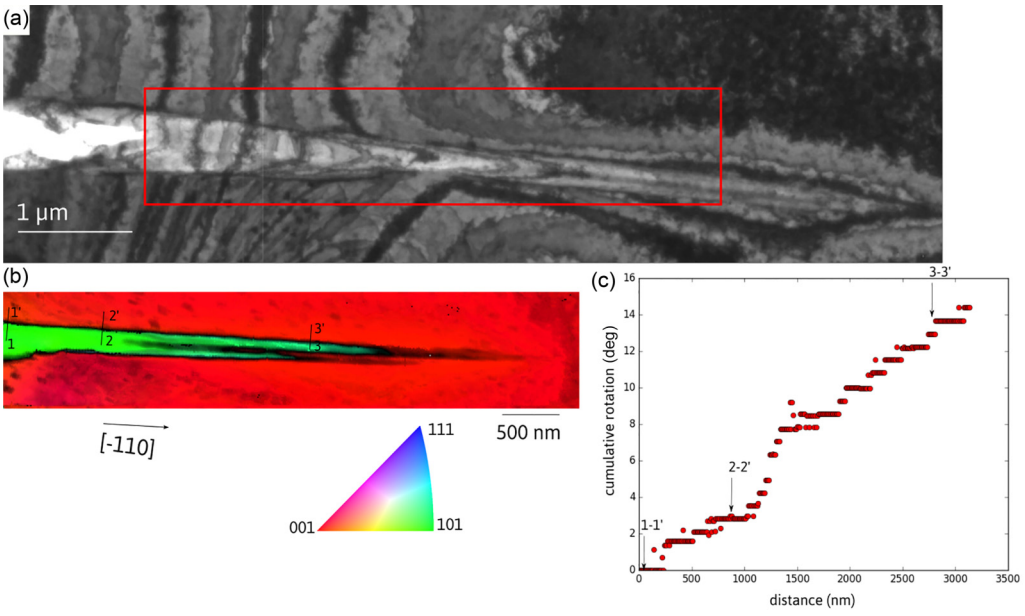

FIG. 9. (a) BF image of a microtwin in front of a crack. (b) The inverse pole figure normal to the foil corresponding to the red area in (a), obtained with ASTAR. The twin corresponds to the green area. (c) The cumulative rotation angle along the twin long direction ($[\bar{1}10]$) starting close to the crack area. Misorientation with the matrix was measured at three locations (i–i').

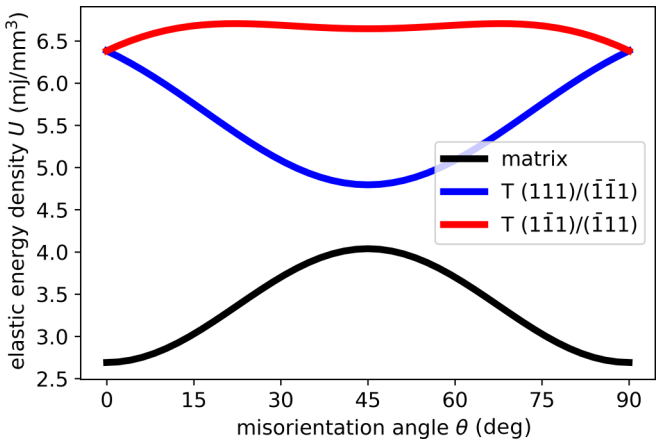

FIG. 10. The elastic energy density for an elastic strain of 1% for the matrix and the four twin families (the results being identical in $T(111)$ and $T(\bar{1}\bar{1}1)$ families, as in $T(1\bar{1}1)$ and $T(\bar{1}11)$), as a function of the misorientation angle θ between the straining direction $[hk0]$ and the [100] direction of the matrix. The [100], [110], [010] straining directions correspond respectively to $\theta = 0, 45, 90°$.

orientation studied in [49]. On the contrary, the present tensile tests should favor detwinning rather than twinning.

A final remark is that U does not depend on the sign of the imposed in-plane strain. Consequently, the above comments apply to a uniaxial compression test. This may partly explain the observed detwinning during unloading, when the sample entered into a compressive stress state.

D. Stress tensors and Schmid factors

The Schmid factors for a [110] loading test are given in the Table I [see also Fig. 1(d) for an illustration of the slip systems with the maximum resolved shear stress and Table A-1 for the Schmid factors of the other tests mentioned in this discussion].

It is seen that the glide systems with the highest Schmid factors correspond to twinning dislocations in the twins that are expanding: $(111)[11\bar{2}]$ and $(\bar{1}\bar{1}1)[\bar{1}\bar{1}\bar{2}]$. Four glide systems associated to perfect dislocations have Schmid factors of 0.41, which, as compared to 0.47 for the primary glide systems, is also large. This explains the observation of perfect dislocations glide along the horizontal directions in the TEM measurements, Fig. 5(b).

We note also that the other glide systems associated to partial dislocations have low Schmid factors and correspond to compression tests. They are therefore probably involved neither in the loading nor in the unloading presented in the results section.

TABLE I. Glide systems and Schmid factors for a [110] uniaxial loading test (very close to a [110] uniaxial straining test). For the $<112>$ directions, the last column indicates if the slip corresponds to a compression (C) or a tension (T) exerted on the sample. The Schmid factors for $(\bar{1}11)$ or $(1\bar{1}1)$ glide planes vanish because the load direction is contained in these planes.

Plane	Direction	m_f	Direction	m_p	C or T
(111)	$[1\bar{1}0]$	0	$[1\bar{2}1]$	0.24	C
	$[10\bar{1}]$	0.41	$[\bar{2}11]$	0.24	C
	$[01\bar{1}]$	0.41	$[11\bar{2}]$	0.47	T
$(\bar{1}\bar{1}1)$	$[\bar{1}10]$	0	$[2\bar{1}1]$	0.24	C
	$[0\bar{1}\bar{1}]$	0.41	$[\bar{1}21]$	0.24	C
	$[\bar{1}0\bar{1}]$	0.41	$[\bar{1}\bar{1}\bar{2}]$	0.47	T

E. Plasticity mechanisms

1. Twinning contribution to the applied strain

During the XRD experiments, the twinning volume increases by a factor of ≈5 for the $T(111)$ and $T(\bar{1}\bar{1}1)$ families for an applied strain of $\varepsilon = 4\%$, Fig. 2. We can give an upper bound on the contribution of the twinning to the plastic deformation of the film. Indeed, in the initial state, the twin volume in the sample is less than 1% (comparing the intensity in the matrix and twin poles), so less than 0.25% per twin family. A complete twinning of the film would induce an elongation of 33% in the [110] direction, as shown in Fig. A-2. Hence, a fivefold increase in the two twin families $T(111)$ and $T(\bar{1}\bar{1}1)$ gives a strain of $2 \times 0.25/100 \times 5 \times 33/100 \approx 0.8\%$. Since the true strain of the film is $\varepsilon = 4\%$ at the end of the loading, the contribution of the twinning mechanism is at most $0.8/4 = 20\%$ of the total strain.

It is also interesting to note that the elastic limit, estimated to an applied strain of $\varepsilon \approx 0.5\%$, corresponds to a longitudinal stress level of $\sigma_{s,xx} \approx 300$ MPa, while the twin volume evolution, appearing at $\varepsilon \approx 1.0\%$, is associated to the flow stress, that is $\sigma_{s,xx} \approx 500$ MPa. Note that these values were obtained from the data in Fig. 4 and Eqs. (A-14) and (A-7) in the SM. As revealed by TEM, twinning nucleation processes are heterogeneous and hence may depend on the type or density of initial defects. This may affect the value of twin volume increase or the twinning critical stress depending on the initial microstructure.

2. Dislocation source

Since, at least in the XRD experiment, the twinning is not the major plasticity mechanism, it is natural to look for dislocation nucleation or multiplication. Tschopp and McDowell showed by molecular dynamics simulations that the $<110>$ axes are those that require the lowest tensile stress for homogeneous dislocation nucleation in copper; moreover, this remains true when we normalize by the orientation-dependent Young modulus [51]. In tension, like in compression, it was partial dislocation loops that were nucleated. In our TEM experiments, we did not observe homogeneous nucleation, but it is most likely due to the high density of defects in the initial state of the films. It is intriguing that we did not observe either heterogeneous dislocation nucleation apart from one Frank-Read source that emitted a single dislocation. In these single crystals, the dislocation sources could come from dislocation reactions, but all the reactions we observed seemed to be without nucleation. Other dislocation sources could be surface steps that appear when cleaving the rock salt substrate for deposition; apparently, these steps had no consequences on the mechanical behavior, at least at the low applied strain imposed here to the film. The dislocations we saw gliding were

initially present: either isolated perfect dislocations, partial dislocations located at ITBs, or twinning dislocations gliding along CTBs.

3. CTB-dislocation interaction

The different modes of CTB-dislocation interactions were described in [52]. The hard modes I and II are characterized by a gliding plane inclined with respect to the CTB, with a gliding direction parallel to the CTB in the second case only. There is also a soft mode, where dislocations are gliding along the CTB. These three modes were observed when a uniaxial compression was applied at 90, 0, and 45° from the CTBs planes, respectively. Many authors confirmed these TB-dislocation interactions, see, e.g., [53].

With respect to the $T(111)$ twin family, dislocations gliding in the (111) planes are in the soft mode, while dislocations gliding in the $(\bar{1}11)$ or $(1\bar{1}1)$ planes are in the hard mode I. We observed indeed some perfect dislocations gliding in the matrix and impinging on a CTB (hard mode I). They were then incorporated into the CTB. After reactions whose details cannot be interpreted at this scale, twinning partials were emitted (soft mode), sometimes with sessile defects. These defects in CTBs may be the source of other dislocations [54] and/or facilitate the CTB migration [55]. Hence, both the hard mode I and the soft mode could contribute to the formation of the large twins observed in Figs. 7(b) and 8.

We note that we never saw a dislocation crossing the two CTBs of a twin, like, e.g., in [53].

4. Microtwin growth and rotation

Figure 8(c) shows a high plastic activity in the large twins. Indeed, numerous slip systems with high Schmid factors are susceptible to being activated in the twinned area, as detailed in Table A-2. Moreover, the plastic events that elongate the film along [110] lead to a local thinning of the film; this in turn entails a stress concentration which localizes the plasticity in a self-sustaining process up to the crack growth. As a result, the fracture profile along the crack in Fig. 8(a) presents numerous ligaments, indicating a large ductility.

The twin rotation quantified with the XRD measurements and observed in the large twins in TEM has the same axis, $[1\bar{1}0]$. Among the slip systems with high resolved shear stress inside a twin from the $T(111)$ family, the glide planes are either (111), $(5\bar{1}\bar{1})$ or $(\bar{1}5\bar{1})$, with respect to the matrix coordinate system. In the first case, it corresponds to dislocations gliding in planes parallel to the CTBs. In the other cases, the dislocations may glide and be stored in the CTBs, which would contribute to the microtwin rotation. We refer the reader to [56,57] for other characterizations and discussions on nanotwins bending.

5. Cracking

First, it is interesting to note that a blocking of crack growth by TBs was noticed in [57–59]; this increased the toughness of the sample. However, this effect was not observed in the present study.

We now discuss the influence of the substrate on the cracking of the films. On the one hand, Figs. 2 and 3 show that the increase in twin volume and the twin rotation occurred simultaneously in the film supported by a substrate; they started at an applied strain slightly larger than 1%, when the elastic strain in the matrix started to decrease. On the other hand, Figs. 7 and 8 show that the increase in twin volume in the freestanding film was important, either in homogeneous areas of the matrix, or close to crack tips, and the twin rotation was observed postmortem also in regions close to crack tips, Fig. 9. Hence, from these two complementary measurements, it seems that the expansion of the growth twin and their rotation go in pairs with the propagation of cracks in the film.

There is, nevertheless, an important difference in the two tests, namely the presence or absence of a substrate. After their deposition, the films are detached from their original NaCl substrates. They contain at this stage (before the mechanical tests) a significant number of defects, which are sources of stress concentrations. When transferred on a TEM grid, the films are freestanding on a large scale, and the initial microstructure heterogeneities have a huge impact. For example, it is seen in the left parts of Figs. 8(a) and 8(b) that many nanotwins kept their original size close to the growth of a micron-sized twin; one image is zoomed in in Fig. A-3. On the contrary, it is well known that a compliant substrate (as the polyimide used in the XRD experiments) prevents, or at least delays, the strain localization that promotes debonding and cracking. This was shown with finite-element simulations [60,61] and has been confirmed experimentally many times [62–64]. In [63], the measured conductivity of the copper film agrees very well with theoretical predictions on continuous films up to a strain larger than 20%. It is therefore questionable that the pristine roughness and porosity of the film have such serious consequences on the hundreds of micrometer-scale properties of the film as probed with x-ray diffraction. For supported thin films, it was suggested in [65] that, far from porosities, dislocations could be nucleated at surface or interface steps and, stopped at and stored in CTBs, contributed to the twin rotations.

Finally, in Fig. 7(a), the nanotwins elongate on both sides; this is another evidence of an ITB migration mechanism independent of the fracture. The elastic repulsion between ITBs, as shown in [66] for the {112} ITBs, could be the driving force and needs further studies.

V. CONCLUSION

Gold single-crystalline 50 nm thin films were studied. Before the tests, the films contained twins a few tens of nanometers long, less than 10 nm thick. The films were uniaxially strained on a polyimide under x-ray diffraction or uniaxially loaded (the in-plane stress ratio R_σ, defined by $\sigma_{s,yy}/\sigma_{s,xx}$, vanishes) in a free-standing configuration in a transmission electron microscope. In gold, a [110] straining induces a value of $R_\sigma = -0.028$ only, so [110] straining and [110] loading tests are very similar.

The combination of the two techniques makes it possible to associate precise quantification of nanotwins evolution (thanks to *in situ* XRD diffraction) with elementary mechanisms identification (thanks to *in situ* TEM). Despite the strong interaction a supported thin film has with its substrate, most of the mechanical behavior seems to be identical for both experiments.

The main results are the following:

(1) In tension, glide of partial dislocations is favored by high values of resolved shear stresses in the (111) and $(\bar{1}\bar{1}1)$ planes. This is in line with the *in situ* XRD measurements, where a 400 to 500% increase of the volume of twins in the $T(111)$ and $T(\bar{1}\bar{1}1)$ families was observed at an applied strain of only 4%.

(2) The twin volume increase is accompanied by a twin rotation around $[1\bar{1}0]$.

(3) However, twinning is not the major plasticity mechanism in the XRD experiment. The elastic limit is around 0.5%, but the twin volume increase starts at around 1.0%. Moreover, the twin contribution to the total strain is at most 20% at the end of the test. This value probably depends on the initial defect type (concerning twins, isolated dislocations, and nanometric holes) and density.

(4) In compression (obtained while unloading thin films supported by substrates with a high elastic limit), perfect dislocations are always favored. The twin volume decreased.

(5) Up to symmetry, the elastic energy associated to a uniaxial in-plane strain test has two particular strain directions: [100], where the four twin families have equal energy, and [110] where the (111) and $(\bar{1}\bar{1}1)$ twin families have an energy much lower than the other two twin families. In any case, from the sole point of view of elastic energy, the anisotropy of the stiffness tensor favors detwinning over twinning in uniaxially strained (001) face-centered cubic thin films.

(6) No dislocation source was monitored in the matrix in *in situ* TEM. Besides the glide of isolated perfect dislocations, we observed, in areas far from initial microstructure heterogeneities, the glide of partial dislocations, either along the CTBs, contributing to the thickening of the twins, or at the front of the ITBs, leading to their migration. This gives the first mechanisms responsible for the twin volume increase.

(7) The twin volume increase may also come from the growth of micron-sized twins in front of crack tips, as observed in TEM. These twins localized the deformation, going in pairs with the growth of ductile cracks. An intense plastic activity developed in these microtwins, probably at the origin of their rotation around $[1\bar{1}0]$, as evidenced by a postmortem TEM orientation map.

ACKNOWLEDGMENTS

The authors gratefully acknowledge SOLEIL for beamtime allocation, Guillaume Geandier for his help during beamtime, and the CNRS network "Microscopie Electronique et Sonde Atomique" (METSA, FR CNRS 3507) for financial support. This work was partially funded by the French Government programs "Investissement d'Avenir" (LABEX INTERACTIFS, Reference No. ANR-11-LABX-0017-01 and EUR INTREE, Reference No. ANR-18-EURE-0010) and Grant No. ANR-19-CE08-0007.

DATA AVAILABILITY

The data that support the findings of this article are not publicly available upon publication because it is not technically feasible, and/or the cost of preparing, depositing, and hosting the data would be prohibitive within the terms of this research project. The data are available from the authors upon reasonable request.

[1] L. Lu, Y. Shen, X. Chen, L. Qian, and K. Lu, Ultrahigh strength and high electrical conductivity in copper, Science **304**, 422 (2004).

[2] L. Lu, X. Chen, X. Huang, and K. Lu, Revealing the maximum strength in nanotwinned copper, Science **323**, 607 (2009).

[3] F. Duan, Y. Lin, J. Pan, L. Zhao, Q. Guo, D. Zhang, and Y. Li, Ultrastrong nanotwinned pure nickel with extremely fine twin thickness, Sci. Adv. **7**, eabg5113 (2021).

[4] M. K. Kini, G. Dehm, and C. Kirchlechner, Size dependent strength, slip transfer and slip compatibility in nanotwinned silver, Acta Mater. **184**, 120 (2020).

[5] X. Ke, J. Ye, Z. Pan, J. Geng, M. F. Besser, D. Qu, A. Caro, J. Marian, R. T. Ott, Y. M. Wang, and F. Sansoz, Ideal maximum strengths and defect-induced softening in nanocrystalline-nanotwinned metals, Nat. Mater. **18**, 1207 (2019).

[6] X. Li, Y. Wei, L. Lu, K. Lu, and H. Gao, Dislocation nucleation governed softening and maximum strength in nano-twinned metals, Nature (London) **464**, 877 (2010).

[7] Q. Fang and F. Sansoz, Columnar grain-driven plasticity and cracking in nanotwinned FCC metals, Acta Mater. **212**, 116925 (2021).

[8] G. Li, Y. Yang, B. Gou, J. Zhang, J. Li, Y. Wang, L. Cao, G. Liu, X. Ding, and J. Sun, Stabilizing defective coherent twin boundaries for strong and stable nanocrystalline nanotwinned Cu, Acta Mater. **241**, 118368 (2022).

[9] T. E. J. Edwards, N. Rohbeck, E. Huszár, K. Thomas, B. Putz, M. N. Polyakov, X. Maeder, L. Pethö, and J. Michler, Thermally stable nanotwins: New heights for Cu mechanics, Adv. Sci. **9**, 2203544 (2022).

[10] T. H. Blewitt, R. R. Coltman, and J. K. Redman, Low temperature deformation of copper single crystals, J. Appl. Phys. **28**, 651 (1957).

[11] T. Mori, H. Fujita, and S. Takemori, *In situ* observations of deformation twinning in Cu-8 at.% Ge single crystals, Phil. Mag. A **44**, 1277 (1981).

[12] B. Hwang, M. Kang, S. Lee, C. R. Weinberger, P. Loya, J. Lou, S. H. Oh, B. Kim, and S. M. Han, Effect of surface energy on size-dependent deformation twinning of defect-free Au nanowires, Nanoscale **7**, 15657 (2015).

[13] R. Béjaud, J. Durinck, and S. Brochard, The effect of surface step and twin boundary on deformation twinning in nanoscale metallic systems, Comput. Mater. Sci. **145**, 116 (2018).

[14] R. Niu, X. An, L. Li, Z. Zhang, Y. W. Mai, and X. Liao, Mechanical properties and deformation behaviours of submicron-sized Cu-Al single crystals, Acta Mater. **223**, 117460 (2022).

[15] A. Sedlmayr, E. Bitzek, D. S. Gianola, G. Richter, R. Mönig, and O. Kraft, Existence of two twinning-mediated plastic deformation modes in Au nanowhiskers, Acta Mater. **60**, 3985 (2012).

[16] Z. Xie, J. Shin, J. Renner, A. Prakash, D. S. Gianola, and E. Bitzek, Origins of strengthening and failure in twinned Au nanowires: Insights from *In-situ* experiments and atomistic simulations, Acta Mater. **187**, 166 (2020).

[17] S. Lee, J. Im, Y. Yoo, E. Bitzek, D. Kiener, G. Richter, B. Kim, and S. H. Oh, Reversible cyclic deformation mechanism of gold nanowires by twinning–detwinning transition evidenced from *in-situ* TEM, Nat. Commun. **5**, 3033 (2014).

[18] A. Catlin, W. P. Walker, and K. R. Lawless, Mechanical twinning in thin evaporated gold films, Acta Metall. **8**, 734 (1960).

[19] J. W. Matthews, Role of deformation twins in the fracture of single-crystal films, Acta Met. **18**, 175 (1970).

[20] P. A. Gruber, C. Solenthaler, E. Arzt, and R. Spolenak, Strong single-crystalline Au films tested by a new synchrotron technique, Acta Mater. **56**, 1876 (2008).

[21] S. H. Oh, M. Legros, D. Kiener, P. Gruber, and G. Dehm, *In situ* TEM straining of single crystal Au films on polyimide: Change of deformation mechanisms at the nanoscale, Acta Mater. **55**, 5558 (2007).

[22] C. Detavernier, A. S. Özcan, J. Jordan-Sweet, E. A. Stach, J. Tersoff, F. M. Ross, and C. Lavoie, An off-normal fibre-like texture in thin films on single-crystal substrates, Nature (London) **426**, 641 (2003).

[23] C. E. Sobrero, C. Lauhoff, T. Wegener, T. Niendorf, and P. Krooß, On the impact of texture and grain size on the pseudoelastic properties of polycrystalline Fe-Ni-Co-Al-Ti alloy, Shap. Mem. Superelasticity **6**, 191 (2020).

[24] J. C. E., Y. Cai, Z. Y. Zhong, M. X. Tang, X. R. Zhu, L. Wang, and S. N. Luo, Texture of nanocrystalline solids: Atomic scale characterization and applications, J. Appl. Cryst. **51**, 124 (2018).

[25] H. Paul, I. Mania, R. Chulist, S. Puchlerska, and M. Prazmowski, On twinning and shear banding in copper single crystals with rolling texture orientations plane strain compressed at high strain rate, Acta Mater. **272**, 119934 (2024).

[26] J. Drieu La. Rochelle, P. Godard, C. Mocuta, D. Thiaudière, J. Nicolai, M. F. Beaufort, M. Drouet, and P. O. Renault, Study of uniaxial deformation behavior of 50 nm-thick thin film of gold single crystal using in situ x-ray pole figure measurements, Surf. Coat. Technol. **377**, 124878 (2019).

[27] M. Legros, F. Mompiou, and D. Caillard, Observing deformation in situ, Nat. Mater. **23**, 20 (2024).

[28] S. H. Oh, M. Legros, D. Kiener, and G. Dehm, *In situ* observation of dislocation nucleation and escape in a submicrometre aluminium single crystal, Nat. Mater. **8**, 95 (2009).

[29] H. Zheng, A. Cao, C. R. Weinberger, J. Y. Huang, K. Du, J. Wang, Y. Ma, Y. Xia, and S. X. Mao, Discrete plasticity in sub-10-nm-sized gold crystals, Nat. Commun. **1**, 144 (2010).

[30] Z. J. Wang, Q. J. Li, Y. Li, L. C. Huang, L. Lu, M. Dao, J. Li, E. Ma, S. Suresh, and Z. W. Shan, Sliding of coherent twin boundaries, Nat. Commun. **8**, 1108 (2017).

[31] N. Lu, K. Du, L. Lu, and H. Q. Ye, Transition of dislocation nucleation induced by local stress concentration in nanotwinned copper, Nat. Commun. **6**, 7648 (2015).

[32] L. Wang, K. Du, C. Yang, J. Teng, L. Fu, Y. Guo, Z. Zhang, and X. Han, In situ atomic-scale observation of grain size and twin thickness effect limit in twin-structural nanocrystalline platinum, Nat. Commun. **11**, 1167 (2020).

[33] See Supplemental Material at http://link.aps.org/supplemental/10.1103/s5l4-z48r for additional information, in particular on the stress and strain tensors in different mechanical tests, on the in-plane strain determination from the measured Bragg peaks shifts, and on the Schmid factors, which include Refs. [20,21,67,68].

[34] https://www.synchrotron-soleil.fr/en/beamlines/diffabs.

[35] P. Pangaud, S. Basolo, N. Boudet, J.-F. Bérar, B. Chantepie, P. Delpierre, B. Dinkespiler, S. Hustache, M. Menouni, and C. Morel, XPAD3: A new photon counting chip for x-ray CT-scanner, Nucl. Instrum. Methods Phys. Res., Sect. A **571**, 321 (2007).

[36] K. Medjoubi, T. Bucaille, S. Hustache, J.-F. Bérar, N. Boudet, J.-C. Clemens, P. Delpierre, and B. Dinkespiler, Detective quantum efficiency, modulation transfer function and energy resolution comparison between CdTe and silicon sensors bump-bonded to XPAD3S, J. Synchrotron Rad. **17**, 486 (2010).

[37] G. Geandier, D. Thiaudière, R. N. Randriamazaoro, R. Chiron, S. Djaziri, B. Lamongie, Y. Diot, E. L. Bourhis, P. O. Renault, P. Goudeau, A. Bouaffad, O. Castelnau, D. Faurie, and F. Hild, Development of a synchrotron biaxial tensile device for *in situ* characterization of thin films mechanical response, Rev Sci Instrum **81**, 103903 (2010).

[38] C. Mocuta, M.-I. Richard, J. Fouet, S. Stanescu, A. Barbier, C. Guichet, O. Thomas, S. Hustache, A. V. Zozulyaa, and D. Thiaudière, Fast pole figure acquisition using area detectors at the diffabs beamline–synchrotron SOLEIL, J. Appl. Cryst. **46**, 1842 (2013).

[39] G. Besnard, F. Hild, and S. Roux, Finite-element displacement fields analysis from digital images: Application to portevin–le châtelier bands, Exp Mech **46**, 789 (2006).

[40] S. Farenc, A. Coujou, and A. Couret, Twin propagation in tial, Mater. Sci. Eng. A **164**, 438 (1993).

[41] A. Sleeswyk, Emissary dislocations: Theory and experiments on the propagation of deformation twins in α-iron, Acta Metall. **10**, 705 (1962).

[42] S. Djaziri, P. O. Renault, F. Hild, E. L. Bourhis, P. Goudeau, D. Thiaudière, and D. Faurie, Combined synchrotron x-ray and image correlation analyses of biaxially deformed W/Cu nanocomposite thin films on Kapton, J. Appl. Crystallogr. **44**, 1071 (2011).

[43] P. O. Renault, T. Sadat, P. Godard, W. He, P. Guerin, G. Geandier, N. Blanc, N. Boudet, and P. Goudeau, Continuous cyclic deformations of a Ni/W film studied by synchrotron x-ray diffraction, Surf. Coat. Technol. **332**, 351 (2017).

[44] P. Godard, A. Guillot, F. Zighem, D. Thiaudière, D. Faurie, and P. O. Renault, Strain ratio and thickness effects on plasticity and crack patterns of nickel thin films, Scr. Mater. **213**, 114638 (2022).

[45] S. A. Husain, P. Kreiml, C. Trost, D. Faurie, M. Cordill, and P. O. Renault, Residual stress and thickness effects on fracture behavior of trilayer films during uniaxial loading, Thin Solid Films **788**, 140173 (2024).

[46] J. H. Seo, Y. Yoo, N. Y. Park, S. W. Yoon, H. Lee, S. Han, S. W. Lee, T. Y. Seong, S. C. Lee, K. B. Lee, P. R. Cha, H. S. Park, B. Kim, and J. P. Ahn, Superplastic deformation of defect-free Au nanowires via coherent twin propagation, Nano Lett. **11**, 3499 (2011).

[47] H. Zhang, M. I. Mendelev, and D. J. Srolovitz, Computer simulation of the elastically driven migration of a flat grain boundary, Acta Mater. **52**, 2569 (2004).

[48] J. Han, S. L. Thomas, and D. J. Srolovitz, Grain-boundary kinetics: A unified approach, Prog. Mater. Sci. **98**, 386 (2018).
[49] H. Xie, G. Wei, Y. Lu, J. Du, F. Yin, G. Lu, and S. Ogata, Driving force of zero-macroscopic-strain deformation twinning in face-centred-cubic metals, Philos. Mag. **101**, 2318 (2021).
[50] A. Vodnick, D. Nowak, S. Labat, O. Thomas, and S. Baker, Out-of-plane stresses arising from grain interactions in textured thin films, Acta Mater. **58**, 2452 (2010).
[51] M. A. Tschopp and D. L. McDowell, Influence of single crystal orientation on homogeneous dislocation nucleation under uniaxial loading, J. Mech. Phys. Solids **56**, 1806 (2008).
[52] Z. You, X. Li, L. Gui, Q. Lu, T. Zhu, H. Gao, and L. Lu, Plastic anisotropy and associated deformation mechanisms in nanotwinned metals, Acta Mater. **61**, 217 (2013).
[53] Q. Lu, Z. You, X. Huang, N. Hansen, and L. Lu, Dependence of dislocation structure on orientation and slip systems in highly oriented nanotwinned Cu, Acta Mater. **127**, 85 (2017).
[54] M. Larranaga, S. Lartigue-Korinek, M. Legros, N. Combe, and F. Mompiou, High temperature plasticity at twin boundary in Al: An *in-situ* TEM perspective, Acta Mater. **251**, 118877 (2023).
[55] M. Larranaga, F. Mompiou, M. Legros, and N. Combe, Role of sessile disconnection dipoles in shear-coupled grain boundary migration, Phys. Rev. Mater. **4**, 123606 (2020).
[56] S. He, B. Jiang, C. Wang, C. Chen, H. Duan, S. Jin, H. Ye, L. Lu, and K. Du, High reversible strain in nanotwinned metals, ACS Appl. Mater. Interfaces **13**, 46088 (2021).
[57] S. Y. He, B. B. Jiang, N. Lu, C. J. Chen, J. P. Cui, Z. Y. Huang, S. Jin, H. Q. Ye, L. Lu, and K. Du, The toughening effect of twins on fracture in nanotwinned Cu during cyclic loading, Acta Mater. **278**, 120232 (2024).
[58] Y. B. Wang, B. Wu, and M. L. Sui, Dynamical dislocation emission processes from twin boundaries, Appl. Phys. Lett. **93**, 041906 (2008).
[59] S. W. Kim, X. Li, H. Gao, and S. Kumar, *In situ* observations of crack arrest and bridging by nanoscale twins in copper thin films, Acta Mater. **60**, 2959 (2012).
[60] T. Li and Z. Suo, Ductility of thin metal films on polymer substrates modulated by interfacial adhesion, Int. J. Solids Struct. **44**, 1696 (2007).
[61] I. Ben Cheikh, G. Parry, D. Dalmas, R. Estevez, and J. Marthelot, Analysis of the multi-cracking mechanism of brittle thin films on elastic-plastic substrates, Int. J. Solids Struct. **180-181**, 176 (2019).
[62] S. P. Lacour, D. Chan, S. Wagner, T. Li, and Z. Suo, Mechanisms of reversible stretchability of thin metal films on elastomeric substrates, Appl. Phys. Lett. **88**, 204103 (2006).
[63] N. Lu, X. Wang, Z. Suo, and J. Vlassak, Metal films on polymer substrates stretched beyond 50%, Appl. Phys. Lett. **91**, 221909 (2007).
[64] M. Melzer, D. Makarov, and O. G. Schmidt, A review on stretchable magnetic field sensorics, J. Phys. D: Appl. Phys. **53**, 083002 (2020).
[65] Y. F. Woguem, Étude par simulations à l'échelle atomique de joints de macle pour les propriétés mécaniques de films minces nano-maclés, Ph.D. thesis, University of Poitiers, France, 2023.
[66] Y. F. Woguem, P. Godard, J. Durinck, and S. Brochard, Elastic energy and interactions between twin boundaries in nanotwinned gold, Comput. Mater. Sci. **228**, 112355 (2023).
[67] G. Simmons and H. Wang, *Single Crystal Elastic Constants and Calculated Aggregate Properties: A Handbook*, 2nd ed. (The MIT Press, Cambridge, 1971).
[68] N. Amiri, F. Tasnim, M. T. Anbarani, C. Dagdeviren, and M. A. Karami, Experimentally verified finite element modeling and analysis of a conformable piezoelectric sensor, Smart Mater. Struct. **30**, 085017 (2021).